





Extreme heterogeneity in the microrheology of lamellar surfactant gels analyzed with neural networks

Owen Watts Moore , Conor Lewis , Thomas Ross , and Thomas Andrew Waigh *

Biological Physics, Department of Physics and Astronomy, The University of Manchester, Manchester M13 9PL, United Kingdom and Photon Science Institute, The University of Manchester, Manchester M13 9PL, United Kingdom

Nickolay Korabel 

Department of Mathematics, The University of Manchester, Manchester M13 9PL, United Kingdom

Cesar Mendoza 

Unilever Research & Development, Port Sunlight Laboratory, Quarry Road East, Bebington, Wirral CH63 3JW, United Kingdom



(Received 21 November 2023; revised 28 March 2024; accepted 22 May 2024; published 2 July 2024)

The heterogeneity of the viscoelasticity of a lamellar gel network based on cetyl-trimethylammonium chloride and cetostearyl alcohol was studied using particle-tracking microrheology. A recurrent neural network (RNN) architecture was used for estimating the Hurst exponent, H , on small sections of tracks of probe spheres moving with fractional Brownian motion. Thus, dynamic segmentation of tracks via neural networks was used in microrheology and it is significantly more accurate than using mean square displacements (MSDs). An ensemble of 414 particles produces a MSD that is subdiffusive in time, t , with a power law of the form $t^{0.74 \pm 0.02}$, indicating power law viscoelasticity. RNN analysis of the probability distributions of H , combined with detailed analysis of the time-averaged MSDs of individual tracks, revealed diverse diffusion processes belied by the simple scaling of the ensemble MSD, such as caging phenomena, which give rise to the complex viscoelasticity of lamellar gels.

DOI: [10.1103/PhysRevE.110.014603](https://doi.org/10.1103/PhysRevE.110.014603)

I. INTRODUCTION

Particle tracking microrheology (PTM) has emerged in the past 30–40 years as a standard tool for probing the microstructure and linear rheology of soft viscoelastic fluids [1]. Compared to bulk rheology experiments, a much larger frequency range can be accessed in a single PTM experiment while using much less fluid [2]. PTM techniques are diverse in their methodology, but all use the random, thermally driven, motion of probe particles suspended in a solvent to discern the rheological properties of the sample [1]. Modern PTM techniques can broadly be split into two categories: passive and active. In passive microrheology, the motion of the probe particles is studied in the absence of an external driving force. Such methods include diffusing wave spectroscopy (DWS) [2], laser deflection particle tracking (LDTP) [3], and video PTM [4–6]. Active microrheology methods, such as magnetic tweezers [7], use an external force to move the probe particle, while the fluid-dependent response is recorded. The fundamental measurement made in PTM experiments is the mean

squared displacement (MSD), $\langle r^2 \rangle$, of the particles' motion [1]. In a viscous fluid, the MSD is related to time, t , via the equation

$$\langle r^2(t) \rangle = 2nDt, \quad (1)$$

where D is the diffusion coefficient and n is the number of dimensions [1,8]. The use of the MSD in this context and its linearity in time was devised by Einstein in his landmark 1905 paper [9]. Ninety years later, Mason and Weitz (1995) derived a method for calculating the viscoelastic spectrum, $\tilde{G}(s)$, from $\langle r^2 \rangle$ in the Laplace domain [2],

$$\tilde{G}(s) = \frac{k_B T}{\pi a s \langle \tilde{r}^2(s) \rangle}, \quad (2)$$

where s is the Laplace frequency, a is the tracer particle radius, $k_B T$ is the thermal energy, and a tilde corresponds to a variable in the Laplace domain. This an expression of the generalized Stokes-Einstein equation and neglects an inertial term that is significant at high frequencies. One consequence of Eq. (2) is that the creep compliance, $J(t)$, is linearly related to $\langle r^2 \rangle$ by a constant of proportionality, without any need to change domains [10,11]:

$$J(t) = \frac{\pi a \langle r^2(t) \rangle}{k_B T}. \quad (3)$$

So long as the size of the probe particles are larger than the largest structure in the fluid [2], this directly links the MSD to bulk linear rheological properties of the fluid. This is often

*Contact author: t.a.waigh@manchester.ac.uk

Published by the American Physical Society under the terms of the Creative Commons Attribution 4.0 International license. Further distribution of this work must maintain attribution to the author(s) and the published article's title, journal citation, and DOI.

inaccessible in complex fluids for mechanical rheometers as fluid microstructures can be fragile and sensitive to deformation. As a result, PTM has been used in a huge variety of media, including living cells [12–15], other biological substances [4–7,16–19], and many nonbiological complex fluids [2,3,20,21]. For reviews of PTM, see Refs. [1,22].

Fluids that do not obey Eq. (1) are said to show anomalous diffusion [8]. A common deviation is for the MSD to follow a power law of the form

$$\langle r^2(t) \rangle \propto t^\alpha, \quad 0 < \alpha < 2. \quad (4)$$

When $\alpha = 1$, the linearity of Eq. (1) for viscous fluids is recovered. The $\alpha < 1$ case is labeled subdiffusion, while $\alpha > 1$ is superdiffusion [8]. Despite its name, anomalous diffusion is very common throughout the sciences [23,24] and naturally arises in stochastic processes defined by the sum of many microscopic events, where the macro-statistics are invariant to the microstatistics [25]. In fluids, subdiffusion can arise from physical or energy barriers temporarily capturing tracer particles or the intrinsic viscoelasticity of the tracer-fluid mixture [26]. Superdiffusion usually requires a driving force. As such, it can often be found in living systems [12,13]. In inanimate nondriven systems, the average behavior at long times is diffusive or subdiffusive to avoid breaking the second law of thermodynamics. For example, it has been detected when associated with fluctuating quantities in complex fluids such as wormlike micelles [21,27,28].

Two of the most common models for anomalous diffusion are the continuous time random walk (CTRW) and fractional Brownian motion (fBm) [29,30]. Though the time dependence of the MSD is similar [Eq. (4)], their mechanisms and the real-world manifestation of their statistics are quite different [31,32]. A CTRW is based on a particle taking discrete jumps. In a decoupled case, it is governed by two independent probability distributions for the jump vector and the time before a jump is made, τ [33]. If the mean of the τ distribution is well-defined, the MSD will follow Eq. (1). If the mean diverges, the process will occur at a slower rate and will be subdiffusive, leading to Eq. (4) [23,26,34]. The distribution in the latter case is nonstationary as large values of τ correspond to a lower probability of making a jump. fBm, $B_H(t)$, is a generalization of Brownian motion to include correlated steps [35]. The covariance function of fBm has the form $\mathbb{E}[B_H(t)B_H(s)] = \frac{1}{2}(|t|^{2H} + |s|^{2H} - |t-s|^{2H})$, such that for $t = s$, $\langle r^2 \rangle \propto t^{2H}$ with $0 < H < 1$. Accordingly, the ranges $0 < H < 1/2$ and $1/2 < H < 1$ correspond to subdiffusion and superdiffusion, respectively. In the language of fBm, these regimes are designated as *antipersistent*, where the steps are negatively correlated, and *persistent*, where the steps are positively correlated. The only distribution governing fBm is the step vector, which is stationary for unobstructed motion with a single value of H .

An MSD can also be produced via a time average given by

$$\overline{r^2}(\Delta) = \frac{\int_0^{T-\Delta} [\mathbf{r}(t+\Delta) - \mathbf{r}(t)]^2 dt}{T-\Delta} \quad (5)$$

in the continuous case. The time lag, Δ , is the difference in time between two points in the random walk, while T is the total walk time. Throughout this paper, a bar above a

variable indicates a time average (TA) and angled brackets an ensemble average (EA). TA MSDs provide better signal to noise than EA and are often preferred in situations where there are few tracks available. In Brownian fluids, if T is large, $\overline{r^2}(\Delta)$ will tend to $\langle r^2(t) \rangle$ [36,37]. This is an expression of ergodicity, where, given enough time, a random variable will sample the entire phase space of a system [38]. Many fluids are nonergodic. This can stem from locally varying rheological properties due to spatial heterogeneity [36,39] or an expression of nonstationary dynamics, such as that of τ for the subdiffusive CTRW [37,39–42]. In heterogeneous fluids, probe particles will belong to subensembles based on their environment. If particles are sampled proportionately from every subensemble, then ergodicity will be recovered [36]. Since the only stochastic process governing fBm is stationary, fBm is ergodic [32,35,43]. In complex fluids, fBm has been observed using single-particle tracking [44,45].

Lamellar gel networks (LGNs) are complex, multiphase structures, e.g., hair conditioners or pharmaceutical creams [46]. They contain a lamellar gel phase made up of bilayers of surfactant and fatty alcohol separated by water, bulk water, and crystals of hydrated fatty alcohol [46–48]. At rest, their microstructure is highly heterogeneous and anisotropic, leading to elastic behavior [46,49,50]. The rheology of such samples is very rich in phenomena and, consequently, poorly understood [51], e.g., hysteresis, shear banding, and wall slip are observed as characteristic of soft-glassy rheological materials. This paper contains an analysis of the dynamics of an LGN based on cetyltrimethylammonium chloride (CTAC) using video particle-tracking microrheology. Both time- and ensemble-averaged MSDs are used, revealing a diverse microenvironment producing subdiffusion on average. A recurrent neural network (RNN) method for estimating the local Hurst exponent based on the feedforward neural network of Han *et al.* (2020) [52] is then used to analyze the local motion of the probe particles. We have combined single- and multioutput neuron models to improve the accuracy of the model for low Hurst exponents. The response of the combined model to simulations is first detailed before the method is applied to heterogeneous dynamics in LGN. Experiments have been chosen that highlight the rich phenomenology governing diffusion in lamellar gel networks.

II. MATERIALS AND METHODS

A. Samples

The LGN used in these experiments is based on a 3:1 ratio of CTAC to cetostearyl alcohol. Other components are demineralised water, versene N_2 crystals (a salt), and a preservative, Kathon CG. This was provided by Unilever and prepared according to the European patent by Casugbo *et al.* (2014) [53] and also Cunningham *et al.* (2021) [54]. Identical samples were previously studied in optical coherence tomography nonlinear rheology experiments [51]. To perform PTM, microparticles must be suspended in the fluid. For this purpose, carboxyl latex microbeads with a diameter of 0.5 μm (ThermoFisher Scientific) and 3×10^8 carboxyl groups per sphere surface were chosen. Particles larger than this were found to appear static due to the elasticity of the LGN, and the finite resolution of our microscope to measure particle

displacement (~ 10 nm). If directly mixed with the LGN, the beads readily aggregate complicating the measurements. To avoid this, long chains of poly(ethylene glycol) (PEG) were added to the surface of the beads by covalent bonds with the surface carboxyl groups, a process called PEGylation. The exact method followed can be found on p. 560 of Hermanson (2013) [55]. Hydrophilic PEG stabilizes the particles in suspension by covering them in flexible polymers that provide a repulsive steric potential that is entropic in origin. This repulsive steric potential limits aggregation of particles [55–58].

Once PEGylated, the spheres were added to the LGN. The elasticity of the LGN at rest precludes standard methods of homogenization, such as sonication, or the use of a centrifuge. Instead, a vortex mixer was used for 5 min to fully suspend the spheres. 10–20 μ l of the suspension was then placed on microscope coverslips and sealed with adhesive spacers. Once sealed, the sample was left for several hours before use to allow any residual mechanical stresses that may have been introduced during preparation to fully relax.

B. Particle-tracking microrheology

Samples were loaded onto an Olympus IX-71 inverted microscope and illuminated by a CoolLED pE-100 light source. The particles were viewed through a 100x immersion oil lens and their motion was recorded on a Photron Fastcam PCI camera. The whole microscope is mounted on an AVI350M dynamic vibration isolation system to reduce the impact of ambient vibrations combined with a sheet of acoustic isolation foam and a large floated optical table. Videos were taken at frame rates in the range 50–10,000 fps to access as large a range of timescales as possible. The particles were then tracked using an in-house program, POLYPARTICLETRACKER, written in MATLAB by Rogers *et al.* (2007) [59]. This software fits a 2D, fourth-order polynomial, weighted by a Gaussian, to each particle. This tracking method is reasonably flexible with respect to particle shape and also intrinsically insensitive to the image background, while providing subpixel accuracy on particle position.

C. Recurrent neural network

Han *et al.* (2020) used a deep learning feedforward neural network (DLFNN) trained on fBm to study the intracellular motion of both endosomes and lysosomes [52] via dynamic segmentation of tracks. Building on this work, we have made a RNN to estimate the Hurst exponent in 15-step segments of fBm tracks. RNNs are known to be well-suited to sequential time-series data due to their ability to remember past data, which is crucial for non-Markovian processes [60,61]. Our RNN has five hidden layers, and a single output neuron that gives a continuous value for the estimated H , H_{est} . The model was trained on 10 000 instances of 15-step fBm created with random simulated H exponents, H_{sim} , generated using the Hosking method [62]. fBm was chosen over other anomalous diffusion processes because of its applicability on the microlevel and its compatibility with the regularly sampled time steps produced in video PTM experiments. The RNN model hyperparameters, including layer structure, activation function, number of neurons, and dropout rate, were chosen

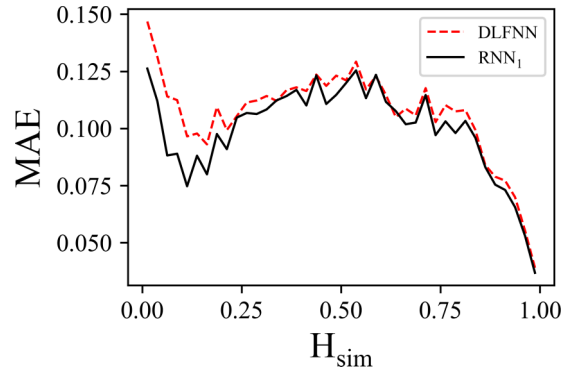


FIG. 1. Mean absolute error (MAE) as a function of the simulated Hurst exponent, H_{sim} , for the DLFNN used by Han *et al.* and our RNN. The values H_{sim} have been binned into intervals 0.02 wide. The mean difference between H_{est} and H_{sim} was then calculated to produce the MAE. Both models have been trained on the same 10 000 2D fBm tracks.

via a Bayesian optimisation [63] routine with 700 iterations, each using the same 10 000 tracks.

The DLFNN used by Han *et al.* was trained on 1D fBm. However, the video PTM data collected here is 2D, so to match the model to the experiment, we have used 2D training data composed of two fBm simulations with the same length and value of H_{sim} . This small change alone decreases the overall mean absolute error (MAE) of the DLFNN method by $\sim 20\%$ for a model with 15 steps. Switching to an RNN from the DLFNN brings an additional 6% improvement in MAE from 0.1060 to 0.0993. Figure 1 shows how the MAE varies with H_{sim} for the 2D DLFNN and RNN. Before the tracks are fed into a neural network (NN), they must be normalized to stop step size becoming a factor in prediction. In the 2D case, the overall displacement, $r_i = \sqrt{x_i^2 + y_i^2}$, where x_i and y_i are the displacements of the two simulated tracks after i time intervals, is normalized between 0 and 1. The sequence of step sizes, $r_{i+1} - r_i$, is then calculated and input to the NN.

When using a model with a single output neuron for short tracks, we found that the range of H_{est} was truncated close to $H_{\text{est}} = 0$ and to a lesser extent $H_{\text{est}} = 1$. Similar artifacts are observed using DLFNNs and are responsible for the increase in MAE at low H_{sim} that can be seen in both models in Fig. 1. To avoid this, we created another model with 21 output neurons corresponding to discrete increments of H 0.05 apart and used the two in tandem. The output activation function for this model is a softmax function that gives each neuron a normalized value between 0 and 1, interpreted as a probability that the given neuron represents the closest value of H to the true result. If the average response of all of the output neurons is taken, a response very similar to that of the single output neuron case is recovered. This suggests that the over/under prediction at low and high H stems from trying to recreate the full range of H behavior using a single weight and bias on the output neuron. A simple algorithm was then used to find H_{est} . If H_{1n} and H_{21n} correspond to the prediction by the model with 1 and 21 output neurons, respectively, it can be stated as

- (1) If $H_{1n} > 0.2$: use H_{1n} .
- (2) Else if $H_{21n} < 0.2$: use H_{21n} .
- (3) Else: use H_{1n} .

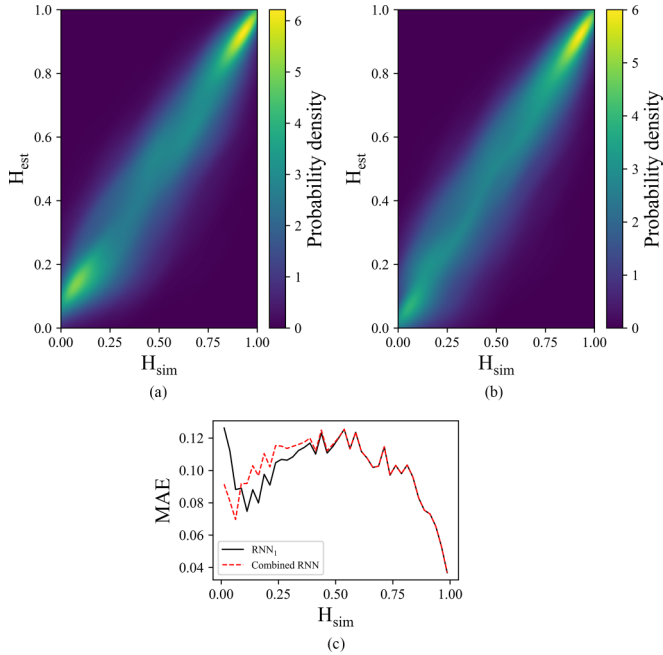


FIG. 2. The Gaussian KDE for the response of the one-neuron and combined models to the same 10 000, 15-step fBm tracks with random H_{sim} are (a) and (b), respectively. The color represents the probability of H_{est} being predicted at a given H_{sim} , with brighter regions corresponding to a larger probability. The mean absolute error, MAE, is plotted as a function of the simulated Hurst exponent, H_{sim} , for each method in (c).

The PC used to train the model also has a small impact on the outcome, so to properly compare models, they must be trained on the same computer and with the same training data. A more detailed discussion of the model architecture and computer can be found in Appendix A 1.

Gaussian kernel density estimate (KDE) plots for each method can be found in Figs. 2(a) and 2(b). They were made using the same 10 000 15-step fBm tracks with random values of H_{sim} . The color on the plot represents the probability of getting a value of H_{est} for a given value of H_{sim} . A gap can clearly be seen at low H_{est} in the one-neuron case [Fig. 2(a)] corresponding to the overshoot previously mentioned. The use of the 21-neuron model for low H estimation [Fig. 2(b)] has filled in this gap, removing the floor for H_{est} . A comparison of the MAE for each method can be seen in Fig. 2(c). The overall MAE increases slightly to 0.1003 for the combined method. This is mostly due to the artificially low error at $H_{\text{sim}} \approx 0.2$ in the 1 output-neuron model, originating from the bunching of the values of H_{est} , increasing the likelihood of a close prediction in that region.

III. RESULTS AND DISCUSSION

A. Simulations

1. Hurst exponent

If a real track moves with fBm, it should be possible to use the distribution of H_{est} to find the true value of H , even if there is a systematic error associated with our model. To provide a measure, fBm tracks with 10 000 steps and single Hurst

exponent, H_{sim} , were simulated and fed into our NN. Given the nonlinearity inherent in NN methods and the bounds on H , it is not clear what type of distribution H_{est} will take. The simplest measures of the shape of a distribution are the first four moments about the mean: mean (μ), variance (σ^2), skewness (μ_3), and kurtosis (μ_4). Because the distributions are nonsymmetric in general, the mean will not necessarily correspond to the peak position. A Gaussian KDE with a bandwidth of 0.075 was therefore used to fit a general nonparametric probability density function (PDF) to each distribution, from which the peak could be estimated. A Gaussian KDE takes the sum of identical Gaussian distributions with centers at each value in the real distribution to create an estimate for the underlying PDF. This has the benefit of requiring no assumptions about the shape of the distribution. However, as Gaussians have no bounds, and $0 < H < 1$, the resulting estimate is not a true PDF. As such, the KDEs used here have been cut off at 0 and 1 and renormalized so the area under the curve is still equal to 1. This has the effect of creating a discontinuity at the extremes for some distributions, as can be particularly seen in Fig. 6(b). Nevertheless, the KDEs provide a good estimate of the peaks in the distributions.

The mean, skewness, and KDE peaks plotted as a function of H_{sim} can be found in Fig. 3. The plots for the variance and kurtosis have been excluded as they have complex, non-monotonic shapes including plateaus and turning points. This means that a single value of σ^2 or μ_4 could correspond to multiple values of H or give H with low accuracy. Given the nonlinear nature of the NN, it is perhaps unsurprising the shape of the distributions produced do not vary smoothly with H_{sim} . Looking at the plot of the mean of the distribution of H_{est} in Fig. 3(a), there are small biases in the prediction stemming from the asymmetry of the distributions. The model seems to work best for $H_{\text{sim}} < 0.5$ as it has been fine-tuned to perform best in the subdiffusive regime, as this is where we expect the majority of motion to be in our LGN. This is mirrored in the skew plot [Fig. 3(b)] where the curve is at its smoothest for $H_{\text{sim}} < 0.5$. The plot of the KDE peak in Fig. 3(c) again shows the best performance for $H_{\text{sim}} < 0.5$ and, in general, produces more accurate results than the mean. To use these plots as a tool for estimating H for real tracks, a cubic spline has been used to interpolate between data points. The results of this can be seen in Table IV for tracks with unimodal distributions of H_{est} .

2. Anisotropy

In the context of fBm, it makes intuitive sense that the anisotropy of a particle's track should be connected to the value of H . If a particle's motion is persistent, it will look more like a straight line the larger H becomes. Conversely, antipersistence will tend to create more symmetrically distributed tracks that change direction often. To test this hypothesis, simulated tracks with a single value of H_{sim} and 500 000 steps were split into sections 45 steps long. Sections containing 45 steps were chosen so as to balance the increasing statistical fluctuation inherent in stochastic tracks with fewer steps and the ability to see local dynamics and provide comparison with the NN estimations of H . A track, sampled N times to give a set of position vectors, can

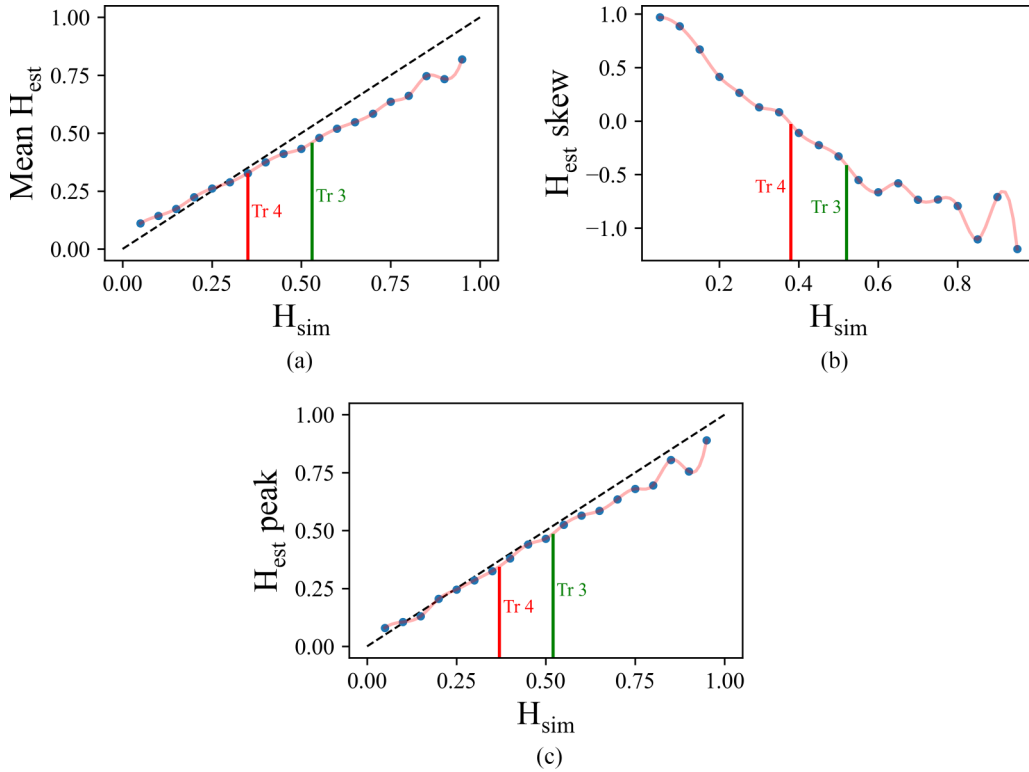


FIG. 3. (a)–(c) show how the mean, skew, and peak position, respectively, of a KDE fit with bandwidth 0.075, of the distributions of H_{est} vary for simulated fBm random walks with 10 000 steps. A cubic spline has been used to interpolate between the data points, and the values of H_{est} suggested for tracks 3 and 4 by their distributions have been plotted in each panel in green and red, respectively. These results are summarized in Table IV. Black dashed lines following $H_{\text{est}} = H_{\text{sim}}$ have been included in (a) and (c) to show where an ideal prediction would be.

be thought of as analogous to a distribution of N identical particles located at each sampled position. This allows the anisotropy to be calculated with the principle moments of the 2D gyration tensor of the track section. The gyration tensor of a distribution of N steps, g_{mn} , is given by

$$g_{mn} = \frac{1}{N} \sum_{i=1}^N r_m^i r_n^i, \quad (6)$$

where r_m^i is the m th spatial coordinate relative to the center of mass of the i th step. The principle moments of g_{mn} are then given by the eigenvalues of the tensor. Working in 2D, there will be two eigenvalues, λ_1 and λ_2 . A circularly symmetric distribution of particles will yield $\lambda_1 = \lambda_2$, while a distribution along a line will result in $\lambda_1 = 0$ (if the coordinate system is chosen such that $\lambda_1 \leq \lambda_2$). The anisotropy, A , can then be normalized to a value between 0 and 1 through the operation

$$A = \frac{\lambda_2 - \lambda_1}{\lambda_1 + \lambda_2}. \quad (7)$$

Since $0 < A < 1$, the same KDE method used for the distributions of H_{est} was again employed here, and plots analogous to those of Fig. 3 for A can be seen in Fig. 4. Each moment varies smoothly with H_{sim} , indicating that the anisotropy is indeed related to H . However, the variance and kurtosis both include extended turning points or plateaus, meaning estimations based on these moments may be inaccurate, so they have again been neglected. The mean,

skewness, and peaks are all monotonic in the main region of interest of $H_{\text{sim}} \lesssim 0.5$, and so should be useful in estimating H . Cubic splines have been used in the same way as Fig. 3 to interpolate the data, aid the eye, and allow for anisotropy to be used to estimate H in real tracks.

B. Hurst exponent and anisotropy

Four tracks that highlight the diversity of behavior present in our LGN samples were chosen, labeled tracks 1–4. Track 1 (T1) was obtained from a data set taken at 50 fps, tracks 2 (T2) and 3 (T3) were taken at 125 fps, and track 4 (T4) at 5000 fps. The tracks with H_{est} overlaid can be seen in Fig. 5. The central point of each 15-step sliding window has been assigned the value of H_{est} output by our RNN. Each track has then been split into 0.1 μm squares and the mean value of H_{est} has been calculated in each square and mapped accordingly.

T1 and T2 [Figs. 5(a) and 5(b)] show clear evidence of caging phenomena where the particle is trapped locally. In both cases, the cages account for a relatively small amount of the spatial extent of the track even though they are the regions in which the particle spends the majority of its time. The cages are on the order of the size of the particles (0.5 μm diameter) and they are interpreted by the neural network as subdiffusive as the particle's motion is tightly bounded, leading to antipersistent behavior. Outside these cages, the motion

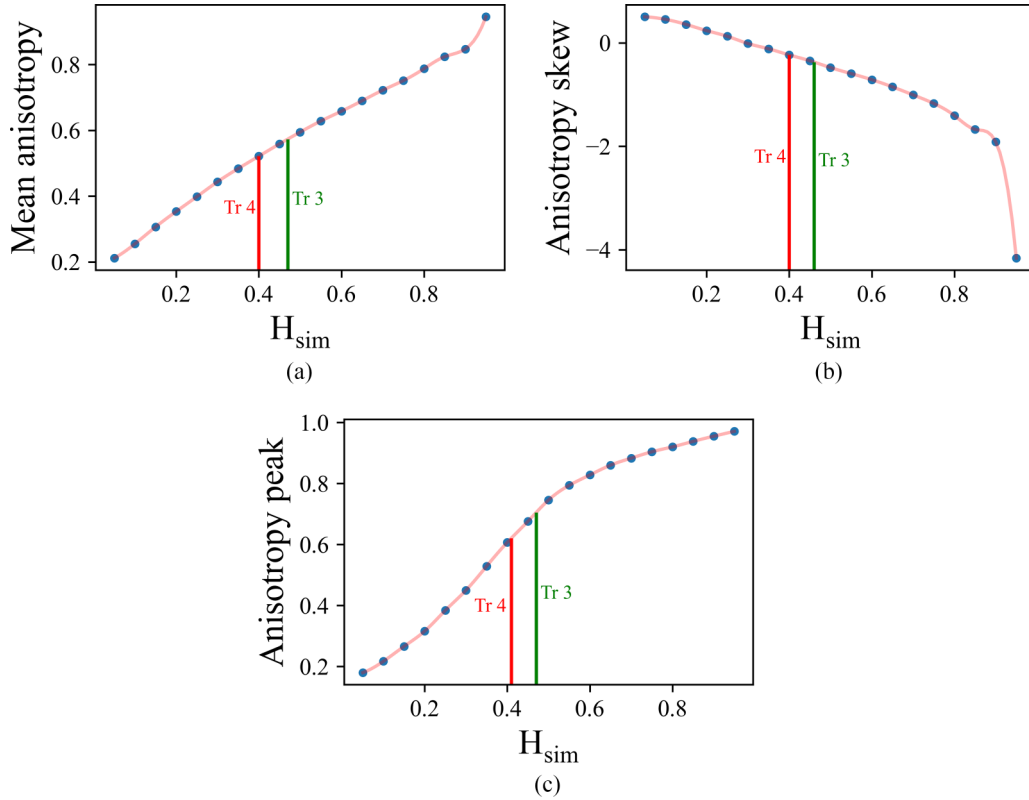


FIG. 4. (a)–(c) show how the mean, skew, and KDE peak of the distribution of anisotropy vary for simulated fBm random walks with different Hurst exponents. Each track has 500 000 steps and a single value of H . The anisotropy is calculated in sliding windows of 45 steps using Eq. (7). The moments can then be calculated from the resulting distribution. A cubic spline has been used to interpolate between the data points, and the values of H suggested by their distributions for tracks 3 and 4 have been plotted on each figure.

of the particles is mostly diffusive or subdiffusive with very local superdiffusive regions. We expect the superdiffusive regions are an expression of the stochastic nature of the motion, since on average there is no driving force for this type of motion. Caging can arise due to particle crowding in concentrated suspensions. The presence of both caging and extended, diffusive, colloidal motion in the same local regions suggests that this isn't the whole story here. There must be structures, be they multilamellar vesicles or lamellar domains, which trap the particles temporarily before they escape into the fluid, which then allows freer movement. Figure 6 shows PDFs for the distributions of H_{est} for T1-4 with Gaussian KDEs fit to each distribution. The effect of the cages in T1 and T2 is reflected in Figs. 6(a) and 6(b), which both show at least two modes in their distribution. The primary peak of the KDE for each are centered at $H_{\text{est}} = 0.285$ and $H_{\text{est}} = 0.225$, respectively. Both tracks have smaller but significant contributions centered at $H_{\text{est}} \approx 0.5$, corresponding to freely diffusive motion. The distributions suggest that the particles are moving in microenvironments with multiple values of H . Alternatively, the presence of a physical environment that hinders the motion of the particles with jumps between neighboring environments suggests that a CTRW-based interpretation may be suitable.

Neither T3 or T4 shows obvious evidence of caging. The motion of T3 is essentially diffusive while T4 is generally subdiffusive. This is backed up by the distributions in Figs. 6(c) and 6(d), which are unimodal. The peaks of the KDE are at

$H_{\text{est}} = 0.490$ and $H_{\text{est}} = 0.340$, respectively, confirming the clear geometrical changes observed in the tracks. T3 appears to show motion in a Newtonian fluid environment, possibly bulk water, while T4 shows motion in a viscoelastic setting. T3 and T4 seem well modeled by fBm. As such, the moments of their distribution warrant comparison with the performance of the NN to fBm simulations summarized in Fig. 3. A cubic spline with increments of H of 0.01 was used to interpolate between the simulation data points. The point that produces the minimum difference between the spline fit and the value of each moment of the distributions for T3 and T4 was then taken as the estimate for the Hurst exponent in each case. The mean estimates for each track are $H_{\text{est}}^{(3)} = 0.523 \pm 0.009$ and $H_{\text{est}}^{(4)} = 0.37 \pm 0.02$, where the uncertainties are the 95% confidence interval. The individual results can be found in Table IV in the Appendix.

To test using the anisotropy as an analytical tool for understanding particle diffusion, T1-4 were treated as in the simulations to produce spatially averaged plots of anisotropy (Fig. 7) and the corresponding distributions (Fig. 8). Gaussian KDEs are again fitted to the plots to aid the eye. Though from the simulations it is clear that anisotropy and Hurst exponent are correlated, the true correlation between the spatially averaged values of H_{est} and the anisotropy is weak at best. This is most likely owing to the large statistical fluctuations present due to the use of short track sections in the estimation of H and calculation of anisotropy. In the cages, we see an exception

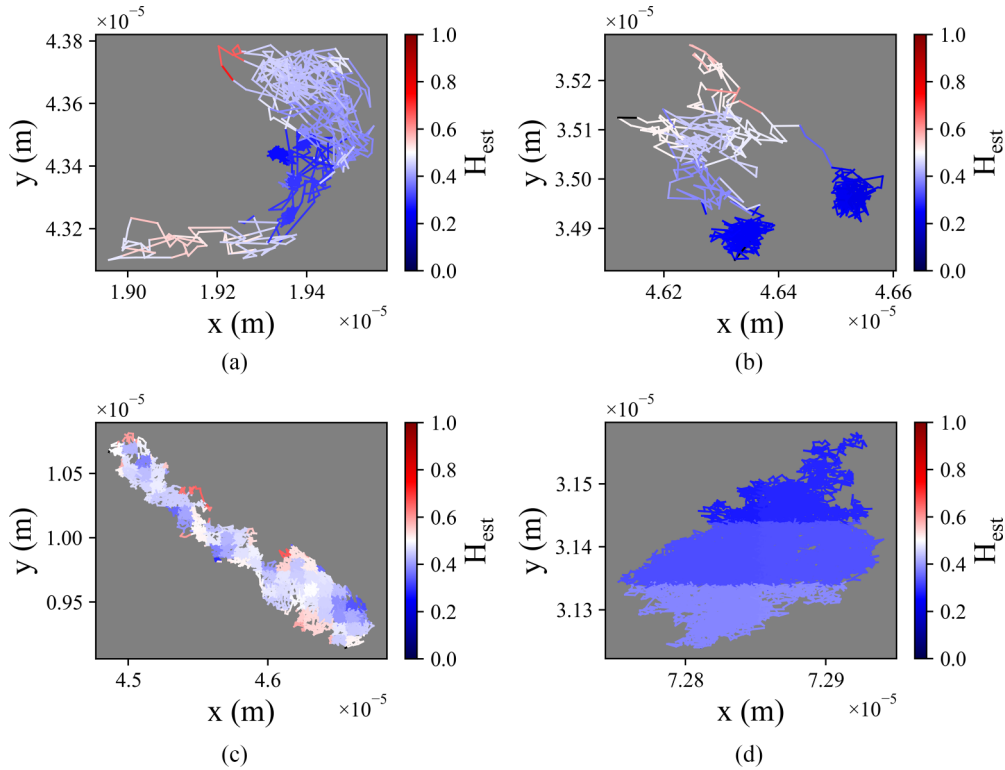


FIG. 5. (a)–(d) Tracks 1, 2, 3, and 4, respectively, with the Hurst exponent mapped. H has been estimated in 15-step sections of each track and then spatially averaged into $0.1 \mu\text{m}$ boxes. Tracks 1 and 2 show clear examples of caging (low H_{est} , subdiffusive regions) where the particle spends the majority of its time. These are surrounded by areas where the particle moves more freely, even becoming superdiffusive. Tracks 3 and 4 show more uniform behavior, 3 moving mostly diffusively and 4 subdiffusively.

to this where the uniformly subdiffusive value of H_{est} is accompanied by regions of low anisotropy. On the distributional level, the similarities are much more obvious. The multimodal distributions of H_{est} for T1 and T2 are replicated in the distributions of anisotropy in Figs. 8(a) and 8(b). The anisotropy distributions of T3 and T4 again mimic their H_{est} counterparts in their unimodal nature and have shapes typical of the distributions obtained in the fBm simulations. The comparison of the four moments of T3 and T4 to simulation can be seen in Fig. 4. The same cubic spline method was used to estimate values of H , giving mean values of $H_{\text{est}}^{(3)} = 0.467 \pm 0.009$ and $H_{\text{est}}^{(4)} = 0.403 \pm 0.009$. The full results are summarized in Table V. These are relatively close to the estimates from the RNN distributions and, to a first approximation, could be used to determine whether a track moving with fBm is subdiffusive. The differences to the RNN most likely stem from the comparatively broad anisotropy distributions and from the imperfect uniformity of the Hurst exponent inherent in real experiments, and in this fluid, in particular. In our fluid, there may also be multiple causes of anisotropy, such as physical blocking, adding further deviation from the results of simulations of free motion.

C. Mean-squared displacement

Nonergodicity naturally leads to a large spread of $\overline{r^2}(\Delta)$ about the ensemble mean [32,41]. However, individual TA MSDs can differ significantly from the ensemble in various ways whether the system is ergodic or not. Confinement in

the interval $[-L, L]$ results in a plateau of the 1D MSD of fBm tracks at $\overline{r^2}(\Delta) = \frac{L^2}{3}$ [32,39,64]. Even though $\langle r^2(t) \rangle$ for subdiffusive CTRW ensembles are sublinear, $\langle \overline{r^2}(\Delta) \rangle$, as well as $\overline{r^2}(\Delta)$ for some tracks, could be linear and so could be mistaken for Brownian motion [32,37,39,41]. In the case of confinement, these linear MSDs will transition to a power law with exponent $1 - \alpha$ at $\frac{L^2}{3}$ [32]. These plateaus can persist to the ensemble average if the confinement is characteristic of the fluid, such as in networks of actin [2,5,65]. MSDs may also be transiently subdiffusive, tending to normal diffusion at long times [3,66]. Mason *et al.* (1997) ascribed this to the relaxation of elasticity within a fluid [3]. In an fBm system, this suggests that there is a timescale beyond which steps are not correlated. Saxton (2007) showed that this behavior can also be produced by a particle in a CTRW in which there is a limit on the maximum depth of the traps (rather than an infinite hierarchy) [66].

Our ensemble of particle tracks includes data sets taken at frame rates of 50, 125, 1000, 2000, 5000, and 10 000 fps. Even though 414 particle tracks have been used in total, the ensemble MSD proved to be noisy, so the ensemble of the TA MSDs was calculated instead. Track MSDs were binned into time intervals and then averaged, resulting in the plot seen in Fig. 9(a). The ensembled data was found to follow a single power law for the whole range of measured time lags: $\langle \overline{r^2}(\Delta) \rangle = (2.42 \pm 0.03) \times 10^{-14} \Delta^{0.74 \pm 0.02}$. The uncertainties here correspond to the 95% confidence interval. The ensemble MSD can be found in Fig. 9(a)(ii) for reference. A

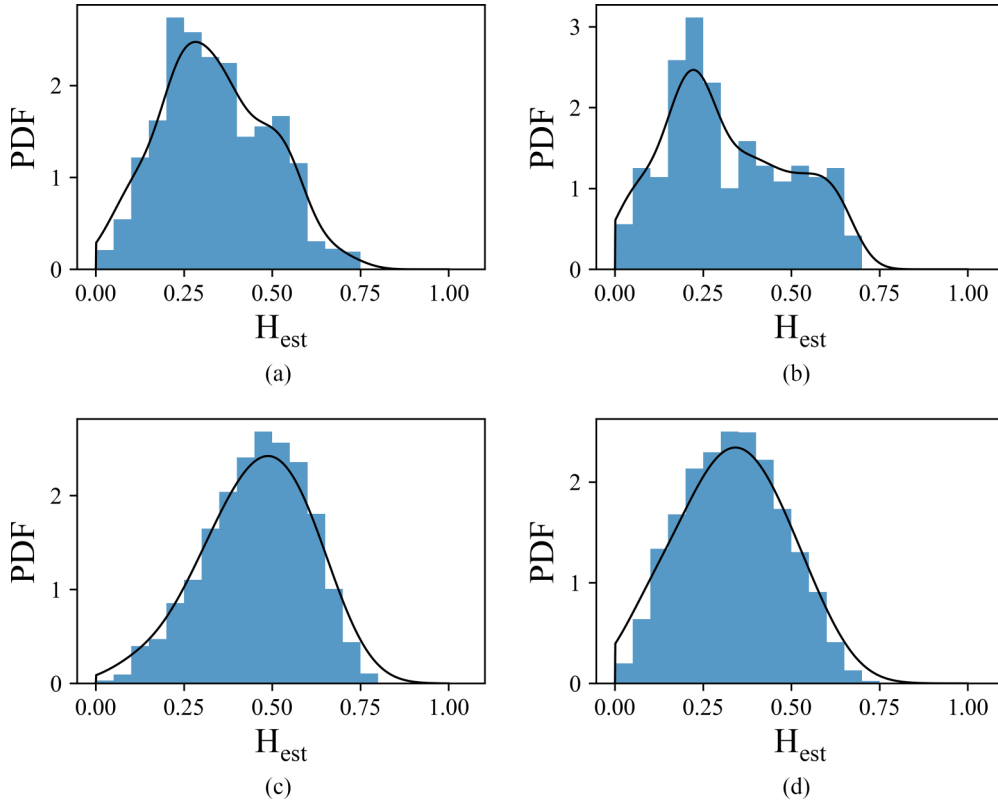


FIG. 6. (a)–(d) Probability density functions (PDFs) for the distribution of the estimated Hurst exponent, H_{est} , for tracks 1–4. The orange curve superposed on each panel is a Gaussian kernel density estimation (KDE) for the PDF. The spatial averages of this can be seen in Fig. 5. (a) and (b) are both multimodal distributions, while (c) and (d) are unimodal. The values of H for the primary peaks of the KDE for (a)–(d) are 0.285, 0.225, 0.490, and 0.340. The secondary peak in (a) comes at $H \approx 0.48$. The secondary peak in (b) is extended with a center at $H \approx 0.5$.

power-law MSD corresponds to a power law $\tilde{G}(s)$ with the same exponent.

Power laws are common in the rheology of complex fluids and are indicative of a broad, continuous, distribution of timescales responsible for stress relaxation or diffusion [67–69]. They appear in soft glassy rheology [67,68] which models the disorder present in a fluid as a distribution of energy barriers corresponding to the energy required to reorganize the microstructure. In response to a macroscopic deformation, the barriers are overcome with a distribution of waiting times corresponding to the distribution of energy barriers, thus sharing conceptual similarities with the CTRW. LGNs such as the one studied in this paper have been shown to exhibit signs of soft glassy rheology [51,70]. Figure 9(a)(i) shows the creep compliance, $J(t)$, for the same fluid sheared in a mechanical rheometer at 3 Pa, below the yield point, recreated from Ref. [51]. The fluid shows power-law dynamics but the bulk and micro behavior don't line up. The bulk power-law exponent is 0.437 ± 0.003 [51] and, if the MSD is converted to $J(t)$ the two curves are still ~ 2 orders of magnitude apart. Understanding this requires a short discussion of the stress-dependent behavior of soft glassy materials (SGMs) and is aided by a comparison with PTM in entangled solutions of F-actin, in which MSDs do not match with the bulk rheology if the particles are too small [71–73].

The behavior of SGMs in response to deformation is analogous to the behavior of glasses in response to changes in

temperature. In place of a critical glass temperature, SGMs have a yield stress. Sheared above this, SGMs act like viscous fluids and are said to be rejuvenated [74]. On the cessation of shear, the structures within the fluid relax, becoming more disordered, increasing the elastic modulus with time. The length of time for which the fluid has been allowed to relax then determines its physical properties in response to shear [74]. This is a function of the processes that have relaxed in the given waiting time. SGMs have two critical stresses: the creep stress and yield stress. Below the creep stress, SGMs act elastically. Above it, limited large-scale deformations occur, causing partial rejuvenation. Above the yield stress, full rejuvenation occurs, eliminating the rheological dependence on waiting time completely [74].

The analogy of SGMs with glasses has led to the creation of time-stress superposition plots (analogous to time-temperature superposition), that allow the study of the rheology of SGMs over long observation times. Cloitre *et al.* (2000) [74] showed that the bulk rheological behavior of an SGM sheared after different waiting times can be superposed by scaling their time axes by a function of the waiting time. Larsen and Furst (2008) [75] used a similar method to investigate the time-dependent gelation of peptide and polyacrylamide gels with PTM. They produced MSDs whose scaling with time lag varied with the time at which data was taken. By scaling the MSD and time lag by empirical factors, they were able to create master curves that accurately

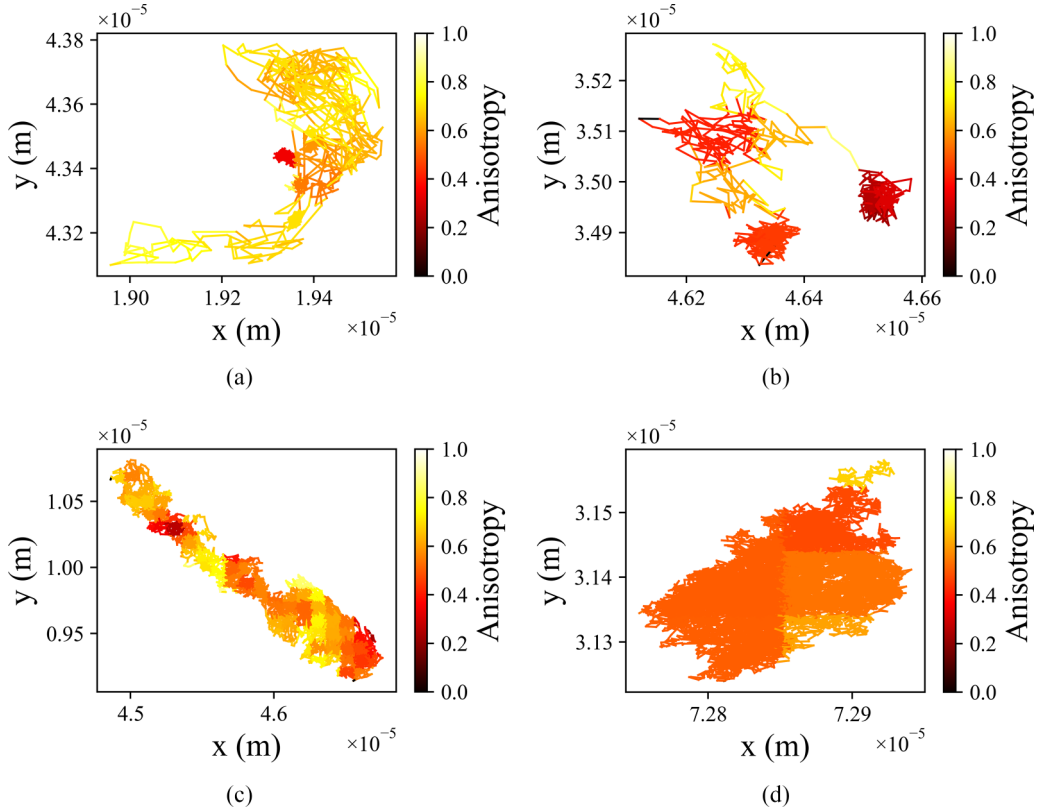


FIG. 7. (a)–(d) Tracks 1–4, respectively, with the anisotropy mapped. The anisotropy was calculated via the ratio of the eigenvalues of the radius of gyration tensor, obtained from Eq. (7). This was for a sliding 45-step window of the track with the value assigned to the point in the center. The anisotropy was then spatially averaged in the same way as in Fig. 5 to produce the figures seen here. Anisotropy = 0 corresponds to circular symmetry and anisotropy = 1 to motion along a straight line. Plots (a) and (b) show striking similarity to their corresponding plots of H , where the subdiffusive, caged regions coincide with areas of low anisotropy, and superdiffusive sections coincide with areas of high anisotropy.

determined the point of gellation. Schultz *et al.* (2012) [76] used the same method to track the degradation of a hydrogel in time and link the change in the elastic modulus with time measured with bulk rheology and PTM. The large discrepancy between the behavior of our MSD and bulk creep compliance measurements could reflect improper scaling of the axes. However, the analyses of Larsen and Furst [75] and Schultz *et al.* [76] relied on the MSDs reflecting the bulk behavior through the generalized Stokes-Einstein equation. It is most likely that the MSDs from our LGN do not meet this criteria.

Entangled solutions of F-actin filaments are a model system for PTM on which much literature has been published [5,17,71–73,77]. It has been shown that the behavior of the MSDs in F-actin vary strongly with the size of the probe particles. For the MSDs from PTM data to match with bulk rheometry, the probes must be larger than both the mesh size and the mean persistence length of the filaments [71–73]. Wong *et al.* (2004) [73] studied anomalous diffusion of microparticles in F-actin and found behavior qualitatively similar to that of our LGN, namely, some particles were constrained throughout the entire observation time and some experienced jumps between different microenvironments. They found that if they only included motion within confined regions in their ensemble MSD and neglected the jumps, their PTM data could reproduce the bulk elastic modulus. Inclusion of the jumps would instead produce a

subdiffusive MSD. This relied on the confined motion having the same viscoelastic character everywhere. In contrast, the neural network analysis of the tracks from our LGN show that a single particle can sample microenvironments with very different viscoelastic properties, suggesting that the bulk behavior is inaccessible with particles of this size. This, in turn, suggests that reconciling the bulk creep compliance with our MSD via a time-stress superposition will be impossible due to the heterogeneity of our LGN.

The bulk creep experiment was conducted with a waiting time of 300 s after shear rejuvenation. Our LGN is known to exhibit thixotropic aging [51], so it is likely that changing the waiting time would have an impact on the rheology. In contrast, the samples in the PTM experiments were purposefully left for a period of a few days to limit the effect of aging on the results due to any rejuvenation that may have occurred from sample preparation. The tracks contributing to the ensemble MSD were taken from different samples, with different waiting times, over a period of several days. Despite this, the MSDs line up well without any need for scaling. This implies the absence of aging, and it is unclear how an empirical scaling for the time axis could be produced under these circumstances. Additionally, if the MSDs were reflecting the bulk behavior of a gel in thermal equilibrium, we would expect the tiny stresses involved ($\sim k_B T/a^2$, where k_B is the Boltzmann constant, T is the absolute temperature,

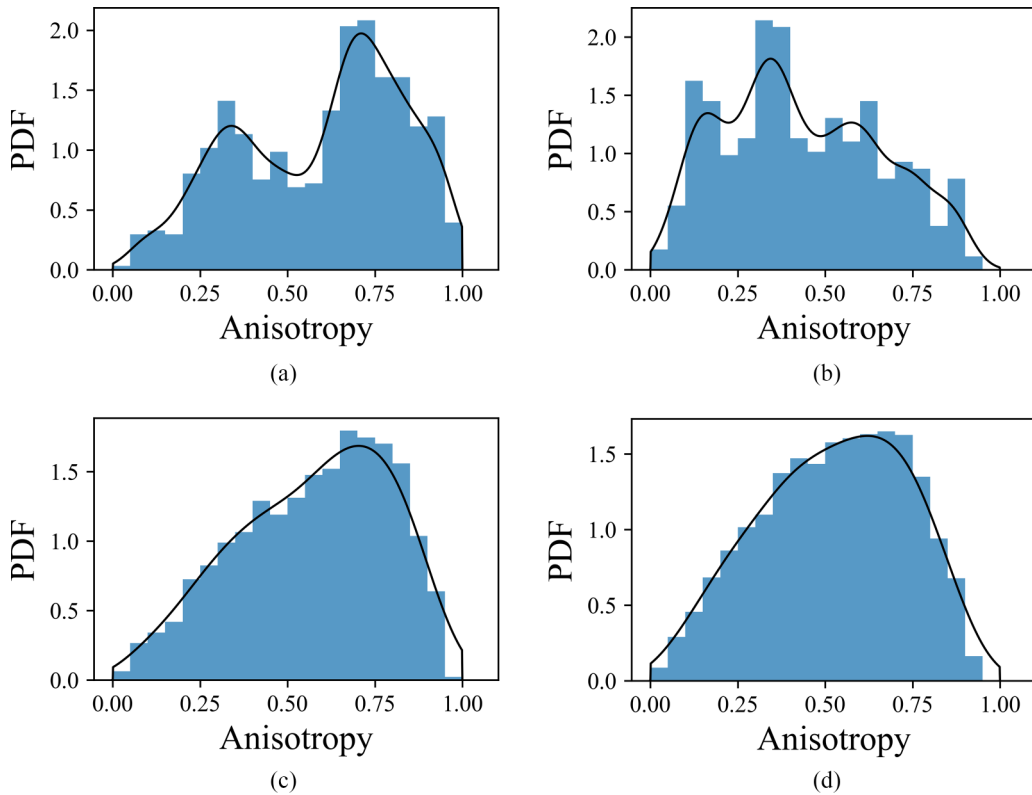


FIG. 8. PDFs of the distribution of anisotropy [Eq. (7)] in tracks 1–4, corresponding to the plots in Fig. 7. The orange line shows a Gaussian KDE for each distribution. From simulations, the anisotropy distribution of tracks with a single Hurst exponent are unimodal. The multimodal distributions seen in (a) and (b) therefore highlight the heterogeneity of the working fluid and should be compared with Figs. 6(a) and 6(b). In contrast, (c) and (d) both closely resemble the distributions of simulated fBm tracks. This further demonstrates that the majority of the motion in these cases is governed by a single Hurst exponent (see their counterpart in Fig. 6).

and a is the particle radius) to produce an elastic plateau. The subdiffusive power law we instead see again suggests we are not accessing bulk behavior and a time-stress superposition would not be possible.

Finally, in the derivation of Eqs. (2) and (3), several assumptions are made, namely, that fluid forms a continuum, without slip, around the tracer particles, that the tracer particles are larger than the largest elasticity causing structure, and

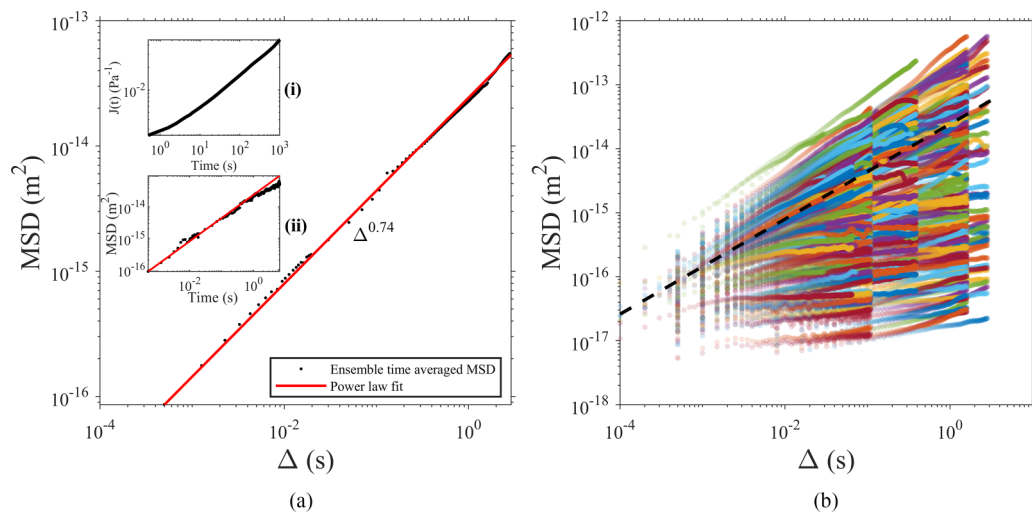


FIG. 9. The ensemble average of the time-averaged MSDs as a function of time lag, Δ , is depicted in (a) with a power-law fit with an exponent of 0.74 ± 0.02 overlaid in red. The uncertainty refers to the 95% confidence interval. Inset (i) shows the results of a creep-recovery experiment conducted with the same fluid, recreated from Watts Moore *et al.* 2023 [51], also showing power-law behavior. Inset (ii) shows the ensemble-averaged MSD with the same power law as the main figure overlaid. The individual time-averaged MSDs as a function of Δ across all frame rates are plotted on the same axes in (b), with the power law for the ensemble overlaid as a black dashed line.

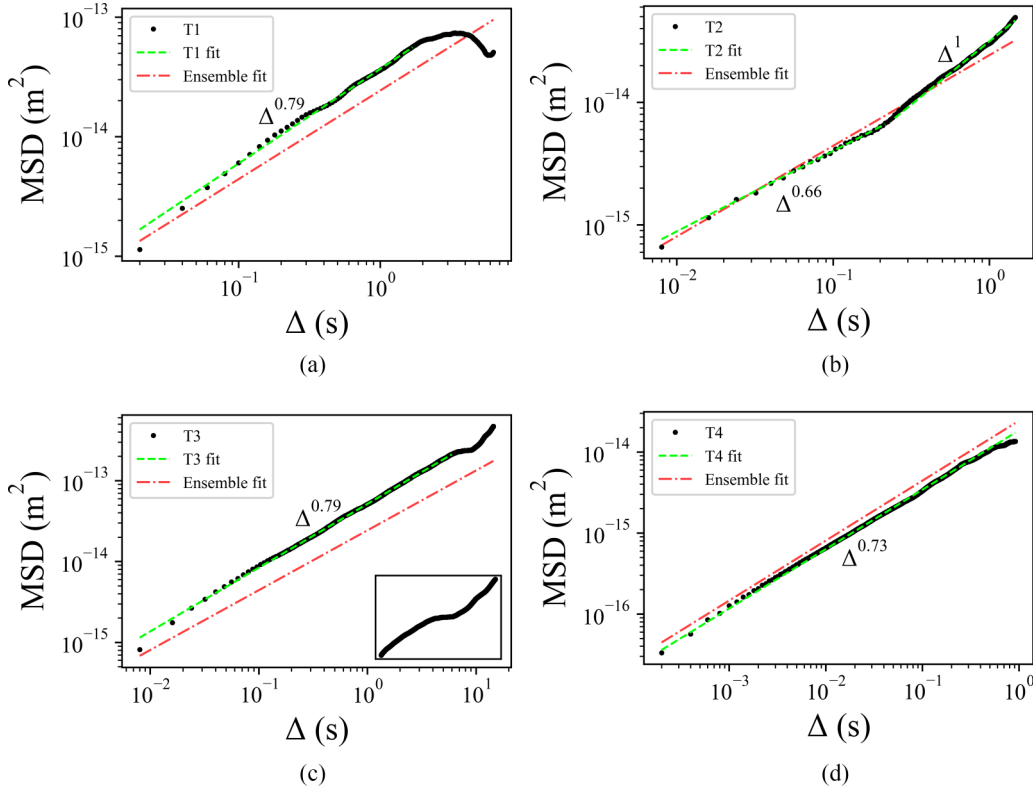


FIG. 10. The TA MSDs of tracks 1–4 as a function of time lag, Δ , can be seen in (a)–(d). A power has been fitted to at least one section of each curve and is displayed as a red dashed line. A blue dashed line represents the power law of the ensemble average of all the TA MSDs. The inset of (c) shows the same MSD plotted on linear scales to highlight the presence of a plateau, often associated with caging phenomena.

that the motion is ergodic [2,3,11]. Images taken via polarized light microscopy reveal that there are spherulites present in the fluid with a size of $\sim 10 \mu\text{m}$ and compound structures that extend over larger length scales still. This is clearly larger than the $0.5 \mu\text{m}$ diameter of the beads. The MSDs in Fig. 9 are therefore not representative of the bulk dynamics of the fluid and are strongly dependent on local behavior and heterogeneity on length scales $\sim 0.5 \mu\text{m}$.

Figure 9(b) shows the individual TA MSDs of all of the particle tracks with the ensemble power law overlaid. It is clear that the spread is large, stretching over several orders of magnitude for a given Δ . Aside from nonergodic dynamics, the spread of the individual TA MSDs can stem from using short tracks and spatially heterogeneous fluids [39]. The length of the tracks in our ensemble are varied, but most have thousands of steps, so a spread this large is unlikely to originate in the track length. It is far more likely to stem from the spatial heterogeneity revealed in our analysis of H and the underlying stochastic dynamics.

Figure 10 shows the TA MSDs for T1–4. After the first few points, T1 [Fig. 10(a)] follows a power law with exponent $\alpha = 0.79 \pm 0.01$ before plateauing, suggesting the motion is confined. In T2, the particle has three modes: two cages and a free section, where the particle moves diffusively. It spends approximately 2 s in each, which means the majority of its time is spent within the cages. The short Δ behavior is therefore dominated by subdiffusive, intracage motion, corresponding to an exponent of $\alpha = 0.66 \pm 0.02$. At longer Δ , the average includes jumps from the cages into the free region,

meaning the displacement is no longer correlated, producing a linear section in the MSD. If the particle were to continue moving between the same three modes for an extended period of time, the MSD would plateau as the average starts to take into account the distance between the cages.

The behavior of T3 again looks subdiffusive, with power-law scaling of the form $\Delta^{0.788 \pm 0.001}$ for short Δ , before a plateau is reached. Though this appears to be in conflict with the NN estimates for H in Fig. 6(c), this apparent subdiffusion is actually an expression of confined Brownian motion. T3 is elongated, which means that we should be able to define its principal axes fairly well using the eigenvectors of Eq. (6). The MSDs in the x and y directions can then be rotated to give the MSDs in the direction of those axes that we will denote a and b through the transformation,

$$\mathbf{EV} \begin{bmatrix} x \\ y \end{bmatrix} = \begin{bmatrix} a \\ b \end{bmatrix}, \quad (8)$$

where \mathbf{EV} is a 2×2 matrix containing the eigenvectors of the gyration tensor. The results of this can be seen in Fig. 11. The MSD for the short axis (MSD_b) of the track quickly plateaus to approximately 10^{-14} m^2 . This corresponds to confinement in the range $2L \approx 0.35 \mu\text{m}$. The MSD for the long axis (MSD_a) starts off in a similar fashion, but when MSD_b plateaus, it keeps increasing, tending to the total MSD. This combination of a plateauing and linear MSD combine to create an overall subdiffusive power law. The plateau in the overall MSD at approximately $2 \times 10^{-13} \text{ m}^2$ corresponds entirely to motion in the a direction. The length scale of confinement to

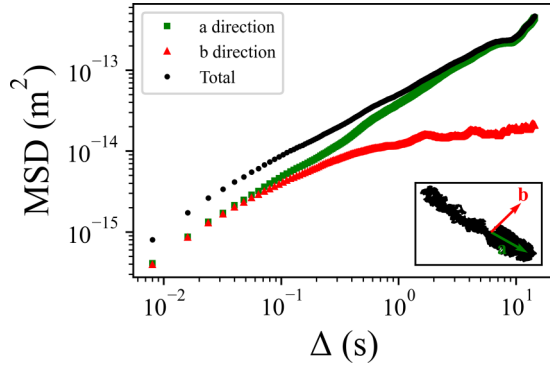


FIG. 11. TA MSD as a function of time lag for T3 split into orthogonal components corresponding to the principal axes of the track, a and b . The track with the direction vectors of each axis labeled is shown in the inset.

produce this plateau is $2L \approx 1.55 \mu\text{m}$. The values of L obtained from the plateaus correspond well with the dimensions of T3 and the shape of the curves in Fig. 11 can easily be reproduced through simulations of Brownian motion with asymmetric physical constraints. T4 closely follows a power law with $\alpha = 0.733 \pm 0.003$ for the majority of its MSD. The lack of deviations suggests that the motion is unconstrained and subdiffusive. As with the distribution of H , this suggests that the motion of T3 is well described by fBm. Using the relation $\alpha = 2H$, the exponent suggests $H \approx 0.37$, closely mirroring the estimates based on the distributions of H_{est} in Fig. 6(d).

D. Discussion

Apgar *et al.* (2000) and Tseng and Wirtz (2001) used the distribution of the dimensionless quantity [5,6],

$$\xi = \frac{\overline{r^2(\Delta)}}{\langle r^2(\Delta) \rangle}, \quad (9)$$

to quantify the heterogeneity of probe particle displacements in actin. For CTRWs, the PDF of ξ should follow a Lévy distribution [41], while for fBm, the distribution should be Gaussian [39]. These relationships hold, even for short tracks, so the distribution can be a key tool in deciphering the dynamics of a system [39]. The PDF of ξ for our tracks at $\Delta = 0.02$ s can be seen in Fig. 12. The PDF has a peak at $\xi = 0$ followed by a long-tailed decrease. The shape of the PDF corresponds to the asymmetry of the spread of individual MSDs around the ensemble in Fig. 9, both of which are hallmarks of nonergodic dynamics [39]. Since the ensemble-time-averaged MSD and the ensemble-averaged MSD have the same power-law exponent (see Fig. 9), we conclude that the origin of this nonergodic behavior is in the heterogeneity of dynamics [78]. However, some nonergodicity could also stem from the superposition of CTRW-like and fBm-like dynamics.

Other attempts to quantify the heterogeneity in PTM tracks have been made by Valentine *et al.* (2001) [77] and Savin and Doyle (2007) [79]. Valentine *et al.* were motivated by the desire to separate the rheological behavior in different microenvironments and quantify the degree to which variation between time-averaged MSDs could be attributed to true heterogeneity as opposed to finite experimental time.

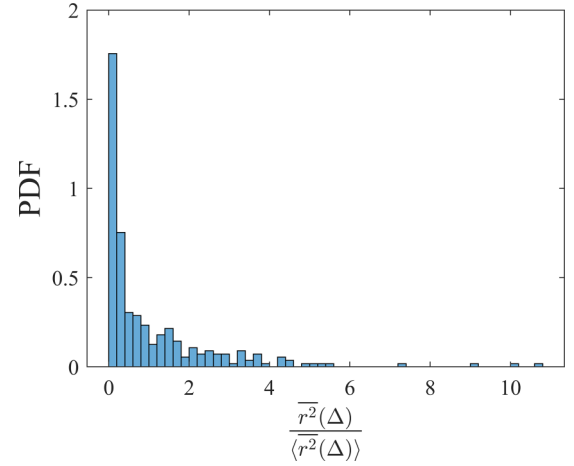


FIG. 12. The PDF of the dimensionless quantity, $\xi = \frac{\overline{r^2(\Delta)}}{\langle r^2(\Delta) \rangle}$, that quantifies fluctuations in the MSD at a time lag of $\Delta = 0.02$ s.

They constructed probability distribution of displacements at a given time lag, both for the ensemble and individual tracks. A Gaussian distribution for the ensemble is indicative of Newtonian behavior, while the variance of the individual track distributions is related to the diffusion coefficient. A homogeneous, viscous fluid would therefore produce tracks with close to identical distributions at a given time lag. A fluid with structure in which particles are permanently trapped would instead give a non-Gaussian ensemble distribution, and individual tracks would have a range of variances according to the dynamics of their microenvironment, influenced by the local viscoelasticity and nature of the cage. By comparing the variances, the tracks can be sorted into clusters with identical dynamics, allowing the properties of the different microenvironments to be probed using the ensemble MSD of the tracks in a given cluster. In fluids where the caging is transient, there can be some ambiguity in the results. In their study of actin, Valentine *et al.* [77] found that the ensemble distribution was approximately Gaussian for short displacements, deviating slightly on larger scales. They were also unable to differentiate between microenvironments, attributing this to particles sampling multiple microenvironments within a single track.

There is a sampling bias inherent in the application of video PTM to heterogeneous fluids. The time for which a particle remains in the volume of observation, defined by the height and width of the microscope image and the depth over which the particle remains in focus, is dependent on the conditions of the microenvironment. Regions with larger viscosity, or stricter confinement, will provide longer tracks, biasing the resulting MSD, especially at long time lags. Savin and Doyle [79] devised estimators of the ensemble MSD and spatial variance of the ensemble MSD that are free from this bias so long as the ratio of tracks with a measured position at a given time lag to the total number of tracks is above a threshold. The variance can then be used to quantify the spatial heterogeneity in an ensemble of tracks.

The behavior of the particles in our LGN seems to be similar to that described in actin by Valentine *et al.* [77], in that multiple microenvironments can be sampled in a single track. Whereas their clustering method failed to resolve this, our RNN can produce maps showing the diversity of the local

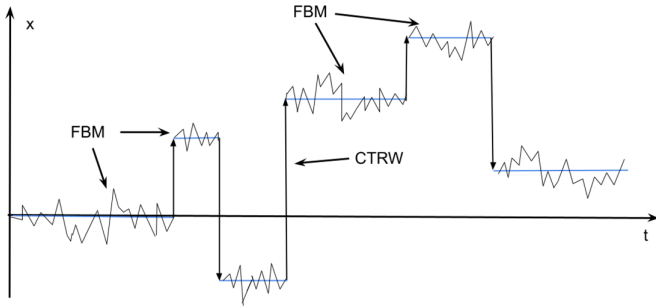


FIG. 13. A sketch of the compound dynamics of a particle in one dimension, x , as a function of time, t . The motion is represented by a CTRW process with fBm overlaid. On the microscopic scale, only fBm motion can be resolved, e.g., with the NN.

environments traversed by a single particle and differentiate between particle dynamics and confinement (see Figs. 5 and 6). The analysis of a track with the RNN is self-contained. So long as the tracks have at least several hundred steps, tracks with large differences in length can be safely compared (for reference, T1-4 have 1263, 734, 7234, and 18326 steps, respectively). This removes the ambiguity about the origin of the variance between time-averaged MSDs, while avoiding some of the biases inherent in the application of MSD analysis to heterogeneous fluids described by Savin and Doyle [79].

The current paper examines the case of extreme spatial heterogeneity in the microrheology of LGNs with particle tracking. We use a fast camera and the neural network fits a small time window (τ_{win}) of 15 sample points ($\tau_{\text{win}} = 0.0015 - 0.3$ s). Since the fractional Brownian motion model provides power-law scaling of the mean square displacement, we know that the viscoelasticity at the timescale τ_{win} is also a power law (a power-law fluid) due to the generalized Stokes-Einstein relationship, e.g., the compliance scales as the same power law. Thus, our fBm model is compatible with the vast majority of common constitutive models for viscoelasticity since they can be described with piecewise power-law scaling of the compliance, e.g., the Maxwell model, the Kelvin model, standard linear solids, etc. In the limit of low spatial heterogeneity in the microrheology of a sample, a multifractal power law fluid model is possible by down-sampling the tracking data and thus varying τ_{win} at which the viscoelasticity of the sample is probed [24]. This process can be effectively performed with a neural network, since it does not require retraining of the neural network (the same number of points can be input into the neural network). We will explore the ability of the neural network to extract constitutive models for systems with low spatial heterogeneity in future work.

There is clearly a range of dynamic behavior governing diffusion in this LGN that defies categorization into a single homogeneous stochastic framework. The fluctuations of the time-averaged MSDs about their ensemble-averaged quantity point towards heterogeneity [78]. Some tracks, including T1 and T2, appear to show elements of a CTRW—long periods on quasilocalized dynamics with transitions between them. At the same time, locally the movement of less than a micron was observed. So, it makes sense to consider a compound process consisting of CTRW and fBm as illustrated in Fig. 13. The

confined Brownian motion of T3 and unconfined subdiffusion of T4, well described by fBm, show two more examples of different diffusion dynamics. Given the varied behaviors at play, it is slightly surprising that the ensemble average follows a single, well-defined subdiffusive power law. More surprisingly still, the subdiffusion of T4 very closely resembles that of the ensemble, as would be expected from a fluid showing only fBm [39,43].

The combination of MSD data with RNN estimations for H has given us greater insight into the stochastic dynamics of individual particle tracks. The multimodal distributions of H_{est} for T1 and T2 are indicative of an extremely heterogeneous local environment which is responsible for the specific, complex shape of their MSDs. The MSDs of T3 and T4 nominally show similar subdiffusive behaviors for small Δ . However, their distributions of H_{est} reveal quite different dynamics: asymmetrically confined Brownian motion for T3, and unconfined fBm for T4. T3, in particular, could easily be mistaken for standard fBm subdiffusion if only the MSD were taken into account. The RNN has helped to differentiate between the diverse diffusion processes in our LGN. This is a particularly useful tool for understanding the dynamics in complex, heterogeneous fluids in which dynamics strongly depend on the local environment or in situations where there are few particle tracks available.

IV. CONCLUSION

In combination with the analysis of ensemble- and time-averaged MSDs, our use of an RNN for dynamic segmentation in particle-tracking microrheology in a LGN has revealed extreme heterogeneity in the stochastic processes governing its diffusion. Despite the ensemble MSD collapsing to a well-defined subdiffusive power law, CTRW-like behavior, Brownian motion, and subdiffusion well described by fBm are all present, sometimes coexisting within the same particle track within ~ 1 micron of each other. The nonergodicity of the ensemble of particles is pronounced, stemming from both the spatial heterogeneity of the LGN microstructure, causing confined motion, and the presence of intrinsically nonergodic CTRW dynamics. The RNN provides complementary information compared with the MSD, quickly and unambiguously revealing dynamics that may be hard to decipher from single-particle dynamics alone. It has proven to be a useful tool and should become standard in the microrheologist's toolkit going forward. A possible extension would be to adapt the NN to find the generalized diffusion coefficient which would be expected to be a spatially varying quantity in complex, heterogeneous fluids, such as the LGN in this study.

Particle tracks available from The University of Manchester data repository [80]. Neural network models and related files available from GitHub [81].

ACKNOWLEDGMENTS

Many thanks to D. Han, A. Kowalski, and P. Martin for invaluable work and advice allowing this paper's completion. This work was made possible with the support of the EPSRC and Unilever under Grant No. EP/R00482X/1 and the EPSRC under Grant No. EP/V008641/1.

APPENDIX: NEURAL NETWORK

1. NN model architecture

Tables I–III show a summary of the model architectures of the 1-output neuron and 21-output neuron models that gave the minimum MAE from a Bayesian optimization routine. The two most common layer types for RNNs are long short-term memory and gated recurrent unit (GRU), which both allow long-term dependencies to be taken into account without the gradient of the loss function diverging during training [60,61,82]. These can be made bidirectional (e.g., BiGRU), meaning that dependencies of the current data point on both past, as in normal RNNs, and future data points in the time series are taken into account [60,82]. The activation function of a layer is generally a nonlinear, monotonic function in which the combined outputs of the neurons from the previous layer are input to activate neurons in the current layer [83]. The number of neurons is the number of trainable units in a layer. The dropout rate is a mechanism to avoid overfitting and requires a randomly selected proportion of neurons in the layer to ignore during a training batch to prevent the reliance on specific neurons. There are also modelwide parameters that need to be optimized, namely, the model learning rate and batch size. The former is related to the size of the steps taken by the model when minimizing the loss function and the latter is the number of data sets from the training set used in a single iteration.

To ensure that each model can be accurately compared, they must be trained with the same tracks and on the same PC. The PC used was a Microsoft Azure virtual machine with a Linux operating system (Ubuntu 20.1), 4 vcpus, and 32 GB memory. When used in combination with the 1-neuron model, small changes were manually made to the biases on the output neurons of the 21-neuron model to make sure that no values of H were over- or underpredicted.

2. Hurst exponent estimates

Tables IV and V summarize the estimations of the Hurst exponent, H , for tracks 3 and 4 from the moments of the distributions of the anisotropy and H simulations. A cubic spline interpolation was used to find the corresponding value of H_{sim} that would produce a distribution with the same moments. The results of this can be seen in Figs. 3 and 4.

TABLE I. Model architecture for RNN with 1-output neuron obtained using Bayesian optimization.

Layer	Structure	Activation function	Neurons	Dropout rate
1	GRU	selu	101	0.147
2	GRU	relu	94	0.233
3	BiGRU	softsign	178	0.389
4	BiLSTM	selu	261	0.184
5	GRU	selu	104	0

TABLE II. Model architecture for RNN with 21-output neurons obtained using Bayesian optimization.

Layer	Structure	Activation function	Neurons	Dropout rate
1	BiLSTM	selu	172	0.577
2	BiLSTM	relu	476	0.229
3	BiLSTM	tanh	225	0.359
4	GRU	tanh	165	0.160
5	BiLSTM	softplus	189	0

TABLE III. Number of output neurons, output activation function (AF), learning rate (LR), and batch size (BS) for each RNN model.

Output neurons	Output AF	LR	BS
1	linear	0.001	37
21	softmax	0.0008	44

TABLE IV. Estimates for H based on the mean, skewness, and KDE peak (H_m , H_s , and H_{KDE}) of the distributions of H_{est} for T3 and T4.

Track	H_m	H_s	H_{KDE}
3	0.53	0.52	0.52
4	0.35	0.38	0.37

TABLE V. Estimates for the Hurst exponent based on the mean, skew, and KDE peak ($H_{A,m}$, $H_{A,s}$, and $H_{A,\text{KDE}}$) of the anisotropy distributions of T3 and T4.

Track	$H_{A,m}$	$H_{A,s}$	$H_{A,\text{KDE}}$
3	0.47	0.46	0.47
4	0.40	0.40	0.41

- [1] T. A. Waigh, Microrheology of complex fluids, *Rep. Prog. Phys.* **68**, 685 (2005).
- [2] T. G. Mason and D. A. Weitz, Optical measurements of frequency-dependent linear viscoelastic moduli of complex fluids, *Phys. Rev. Lett.* **74**, 1250 (1995).
- [3] T. G. Mason, K. Ganesan, J. H. van Zanten, D. Wirtz, and S. C. Kuo, Particle tracking microrheology of complex fluids, *Phys. Rev. Lett.* **79**, 3282 (1997).
- [4] T. G. Mason, A. Dhople, and D. Wirtz, Concentrated DNA rheology and microrheology, in *Materials Research Society Symposium—Proceedings* (1996), Vol. 463, pp. 153–158.
- [5] J. Apgar, Y. Tseng, E. Fedorov, M. B. Herwig, S. C. Almo, and D. Wirtz, Multiple-particle tracking measurements of heterogeneities in solutions of actin filaments and actin bundles, *Biophys. J.* **79**, 1095 (2000).
- [6] Y. Tseng and D. Wirtz, Mechanics and multiple-particle tracking microheterogeneity of α -actinin-cross-linked actin filament networks, *Biophys. J.* **81**, 1643 (2001).
- [7] F. Ziemann, J. Radler, and E. Sackmann, Local measurements of viscoelastic moduli of entangled actin networks using an oscillating magnetic bead micro-rheometer, *Biophys. J.* **66**, 2210 (1994).
- [8] J. P. Bouchaud and A. Georges, Anomalous diffusion in disordered media: Statistical mechanisms, models and physical applications, *Phys. Rep.* **195**, 127 (1990).
- [9] A. Einstein, On the movement of small particles suspended in stationary liquids required by the molecular-kinetic theory of heat, *Ann. Phys.* **322**, 549 (1905).
- [10] W. A. Petka, J. L. Harden, K. P. McGrath, D. Wirtz, and D. A. Tirrell, Reversible hydrogels from self-assembling artificial proteins, *Science* **281**, 389 (1998).
- [11] T. G. Mason, Estimating the viscoelastic moduli of complex fluids using the generalized Stokes-Einstein equation, *Rheol. Acta* **39**, 371 (2000).
- [12] A. W. Harrison, D. A. Kenwright, T. A. Waigh, P. G. Woodman, and V. J. Allan, Modes of correlated angular motion in live cells across three distinct time scales, *Phys. Biol.* **10**, 036002 (2013).
- [13] A. Caspi, R. Granek, and M. Elbaum, Enhanced diffusion in active intracellular transport, *Phys. Rev. Lett.* **85**, 5655 (2000).
- [14] S. S. Rogers, T. A. Waigh, and J. R. Lu, Intracellular microrheology of motile amoeba proteus, *Biophys. J.* **94**, 3313 (2008).
- [15] D. Wirtz, Particle-tracking microrheology of living cells: Principles and applications, *Annu. Rev. Biophys.* **38**, 301 (2009).
- [16] P. Georgiades, P. D. Pudney, D. J. Thornton, and T. A. Waigh, Particle tracking microrheology of purified gastrointestinal mucins, *Biopolymers* **101**, 366 (2014).
- [17] M. L. Gardel, M. T. Valentine, J. C. Crocker, A. R. Bausch, and D. A. Weitz, Microrheology of entangled F-actin solutions, *Phys. Rev. Lett.* **91**, 158302 (2003).
- [18] J. W. Hart, T. A. Waigh, J. R. Lu, and I. S. Roberts, Microrheology and spatial heterogeneity of *Staphylococcus aureus* biofilms modulated by hydrodynamic shear and biofilm-degrading enzymes, *Langmuir* **35**, 3553 (2019).
- [19] I. A. Hasnain and A. M. Donald, Microrheological characterization of anisotropic materials, *Phys. Rev. E* **73**, 031901 (2006).
- [20] O. D. Lavrentovich, Transport of particles in liquid crystals, *Soft Matter* **10**, 1264 (2014).
- [21] R. Ganapathy, A. K. Sood, and S. Ramaswamy, Superdiffusion of concentration in wormlike-micelle solutions, *Europhys. Lett.* **77**, 18007 (2007).
- [22] T. A. Waigh, Advances in the microrheology of complex fluids, *Rep. Prog. Phys.* **79**, 074601 (2016).
- [23] J. Klafter and I. M. Sokolov, Anomalous diffusion spreads its wings, *Phys. World* **18**, 29 (2005).
- [24] T. A. Waigh and N. Korabel, Heterogeneous anomalous transport in cellular and molecular biology, *Rep. Prog. Phys.* **86**, 126601 (2023).
- [25] I. Eliazar and J. Klafter, Anomalous is ubiquitous, *Ann. Phys.* **326**, 2517 (2011).
- [26] I. M. Sokolov, Models of anomalous diffusion in crowded environments, *Soft Matter* **8**, 9043 (2012).
- [27] A. Ott, J. P. Bouchaud, D. Langevin, and W. Urbach, Anomalous diffusion in “living polymers”: A genuine Levy flight? *Phys. Rev. Lett.* **65**, 2201 (1990).
- [28] Y. Gambin, G. Massiera, L. Ramos, C. Ligoure, and W. Urbach, Bounded step superdiffusion in an oriented hexagonal phase, *Phys. Rev. Lett.* **94**, 110602 (2005).
- [29] E. W. Montroll and G. H. Weiss, Random walks on lattices. II, *J. Math. Phys.* **6**, 167 (1965).
- [30] B. B. Mandelbrot and J. W. Van Ness, Fractional Brownian motions, fractional noises and applications, *SIAM Rev.* **10**, 422 (1968).
- [31] M. Magdziarz, A. Weron, and J. Klafter, Equivalence of the fractional Fokker-Planck and subordinated Langevin equations: The case of a time-dependent force, *Phys. Rev. Lett.* **101**, 210601 (2008).
- [32] S. Burov, J. H. Jeon, R. Metzler, and E. Barkai, Single particle tracking in systems showing anomalous diffusion: The role of weak ergodicity breaking, *Phys. Chem. Chem. Phys.* **13**, 1800 (2011).
- [33] R. Metzler and J. Klafter, The random walk’s guide to anomalous diffusion: A fractional dynamics approach, *Phys. Rep.* **339**, 1 (2000).
- [34] I. M. Sokolov and J. Klafter, From diffusion to anomalous diffusion: A century after Einstein’s Brownian motion, *Chaos* **15**, 026103 (2005).
- [35] I. I. Eliazar and M. F. Shlesinger, Fractional motions, *Phys. Rep.* **527**, 101 (2013).
- [36] P. N. Pusey, Dynamic light scattering by non-ergodic media, *Physica A* **157**, 705 (1989).
- [37] A. Lubelski, I. M. Sokolov, and J. Klafter, Nonergodicity mimics inhomogeneity in single particle tracking, *Phys. Rev. Lett.* **100**, 250602 (2008).
- [38] J. Rudnick and G. Gaspari, *Elements of the Random Walk*, 1st ed. (Cambridge University Press, Cambridge, 2004).
- [39] J. H. Jeon and R. Metzler, Analysis of short subdiffusive time series: Scatter of the time-averaged mean-squared displacement, *J. Phys. A: Math. Theor.* **43**, 252001 (2010).
- [40] G. Bel and E. Barkai, Weak ergodicity breaking in the continuous-time random walk, *Phys. Rev. Lett.* **94**, 240602 (2005).
- [41] Y. He, S. Burov, R. Metzler, and E. Barkai, Random time-scale invariant diffusion and transport coefficients, *Phys. Rev. Lett.* **101**, 058101 (2008).
- [42] S. Burov, R. Metzler, and E. Barkai, Aging and nonergodicity beyond the Khinchin theorem, *Proc. Natl. Acad. Sci. USA* **107**, 13228 (2010).

- [43] W. Deng and E. Barkai, Ergodic properties of fractional Brownian-Langevin motion, *Phys. Rev. E* **79**, 011112 (2009).
- [44] M. Weiss, Single-particle tracking data reveal anticorrelated fractional Brownian motion in crowded fluids, *Phys. Rev. E* **88**, 010101(R) (2013).
- [45] I. Golding and E. C. Cox, Physical nature of bacterial cytoplasm, *Phys. Rev. Lett.* **96**, 098102 (2006).
- [46] T. Iwata, Lamellar gel network, in *Cosmetic Science and Technology: Theoretical Principles and Applications*, edited by K. Sakamoto, R. Lochhead, H. Maibach, and Y. Yamashita (Elsevier Inc., Amsterdam, Netherlands, 2017), Chap. 25, pp. 415–447.
- [47] H. Junginger, Colloidal structures of O/W creams, *Pharm. Weekbl. Sci. Ed.* **6**, 141 (1984).
- [48] G. M. Eccleston, Functions of mixed emulsifiers and emulsifying waxes in dermatological lotions and creams, *Colloids Surf. A* **123-124**, 169 (1997).
- [49] H. Hoffmann and W. Ulbricht, Surfactant gels, *Curr. Opin. Colloid Interface Sci.* **1**, 726 (1996).
- [50] H. E. Warriner, S. H. Idziak, N. L. Slack, P. Davidson, and C. R. Safinya, Lamellar biogels: Fluid-membrane-based hydrogels containing polymer lipids, *Science* **271**, 969 (1996).
- [51] O. Watts Moore, T. A. Waigh, C. Mendoza, and A. Kowalski, Characterizing the rheology of lamellar gel networks with optical coherence tomography velocimetry, *J. Rheol.* **67**, 589 (2023).
- [52] D. Han, N. Korabel, R. Chen, M. Johnston, A. Gavrilova, V. J. Allan, S. Fedotov, and T. A. Waigh, Deciphering anomalous heterogeneous intracellular transport with neural networks, *eLife* **9**, e52224 (2020).
- [53] C. Casugbo, M. Flanagan, J. A. Hough, J. M. Naughton, and D. Serridge, *Composition* (WIPO (PCT), 2014).
- [54] G. E. Cunningham, F. Alberini, M. J. Simmons, and J. J. O’Sullivan, Understanding the effects of processing conditions on the formation of lamellar gel networks using a rheological approach, *Chem. Eng. Sci.* **242**, 116752 (2021).
- [55] G. T. Hermanson, Microparticles and nanoparticles, in *Bioconjugate Techniques*, edited by G. T. Hermanson (Academic Press, Boston, 2013), Chap. 14, pp. 549–587.
- [56] S. I. Jeon, J. H. Lee, J. D. Andrade, and P. G. De Gennes, Protein-surface interactions in the presence of polyethylene oxide. I. Simplified theory, *J. Colloid Interface Sci.* **142**, 149 (1991).
- [57] D. Needham, T. J. McIntosh, and D. D. Lasic, Repulsive interactions and mechanical stability of polymer-grafted lipid membranes, *Biochim. Biophys. Acta, Biomembr.* **1108**, 40 (1992).
- [58] D. D. Lasic, F. J. Martin, A. Gabizon, S. K. Huang, and D. Papahadjopoulos, Sterically stabilized liposomes: A hypothesis on the molecular origin of the extended circulation times, *Biochim. Biophys. Acta, Biomembr.* **1070**, 187 (1991).
- [59] S. S. Rogers, T. A. Waigh, X. Zhao, and J. R. Lu, Precise particle tracking against a complicated background: Polynomial fitting with Gaussian weight, *Phys. Biol.* **4**, 220 (2007).
- [60] Y. Yu, X. Si, C. Hu, and J. Zhang, A review of recurrent neural networks: LSTM cells and network architectures, *Neural Comput.* **31**, 1235 (2019).
- [61] A. Shewalkar, D. Nyavanandi, and S. A. Ludwig, Performance evaluation of deep neural networks applied to speech recognition: RNN, LSTM and GRU, *J. Artif. Intell. Soft Comput. Res.* **9**, 235 (2019).
- [62] J. R. Hosking, Modeling persistence in hydrological time series using fractional differencing, *Water Resour. Res.* **20**, 1898 (1984).
- [63] J. Wu, X. Y. Chen, H. Zhang, L. D. Xiong, H. Lei, and S. H. Deng, Hyperparameter optimization for machine learning models based on Bayesian optimization, *J. Electron. Sci. Technol.* **17**, 100007 (2019).
- [64] J. H. Jeon and R. Metzler, Fractional Brownian motion and motion governed by the fractional Langevin equation in confined geometries, *Phys. Rev. E* **81**, 021103 (2010).
- [65] A. Palmer, T. G. Mason, J. Xu, S. C. Kuo, and D. Wirtz, Diffusing wave spectroscopy microrheology of actin filament networks, *Biophys. J.* **76**, 1063 (1999).
- [66] M. J. Saxton, A biological interpretation of transient anomalous subdiffusion. I. Qualitative model, *Biophys. J.* **92**, 1178 (2007).
- [67] P. Sollich, F. Lequeux, P. Hébraud, and M. E. Cates, Rheology of soft glassy materials, *Phys. Rev. Lett.* **78**, 2020 (1997).
- [68] S. M. Fielding, P. Sollich, and M. E. Cates, Aging and rheology in soft materials, *J. Rheol.* **44**, 323 (2000).
- [69] A. Bonfanti, J. L. Kaplan, G. Charras, and A. Kabla, Fractional viscoelastic models for power-law materials, *Soft Matter* **16**, 6002 (2020).
- [70] A. Datta, V. S. Tanmay, G. X. Tan, G. W. Reynolds, S. N. Jamadagni, and R. G. Larson, Characterizing the rheology, slip, and velocity profiles of lamellar gel networks, *J. Rheol.* **64**, 851 (2020).
- [71] A. C. Maggs, Micro-bead mechanics with actin filaments, *Phys. Rev. E* **57**, 2091 (1998).
- [72] F. G. Schmidt, B. Hinner, and E. Sackmann, Microrheometry underestimates the values of the viscoelastic moduli in measurements on F-actin solutions compared to macrorheometry, *Phys. Rev. E* **61**, 5646 (2000).
- [73] I. Y. Wong, M. L. Gardel, D. R. Reichman, E. R. Weeks, M. T. Valentine, A. R. Bausch, and D. A. Weitz, Anomalous diffusion probes microstructure dynamics of entangled F-actin networks, *Phys. Rev. Lett.* **92**, 178101 (2004).
- [74] M. Cloitre, R. Borrega, and L. Leibler, Rheological aging and rejuvenation in microgel pastes, *Phys. Rev. Lett.* **85**, 4819 (2000).
- [75] T. H. Larsen and E. M. Furst, Microrheology of the liquid-solid transition during gelation, *Phys. Rev. Lett.* **100**, 146001 (2008).
- [76] K. M. Schultz, A. D. Baldwin, K. L. Kiick, and E. M. Furst, Measuring the modulus and reverse percolation transition of a degrading hydrogel, *ACS Macro Lett.* **1**, 706 (2012).
- [77] M. T. Valentine, P. D. Kaplan, D. Thota, J. C. Crocker, T. Gisler, R. K. Prud’homme, M. Beck, and D. A. Weitz, Investigating the microenvironments of inhomogeneous soft materials with multiple particle tracking, *Phys. Rev. E* **64**, 061506 (2001).
- [78] N. Korabel, A. Taloni, G. Pagnini, V. Allan, S. Fedotov, and T. A. Waigh, Ensemble heterogeneity mimics ageing for endosomal dynamics within eukaryotic cells, *Sci. Rep.* **13**, 8789 (2023).

- [79] T. Savin and P. S. Doyle, Statistical and sampling issues when using multiple particle tracking, *Phys. Rev. E* **76**, 021501 (2007).
- [80] O. W. Moore, T. Waigh, N. Korabel, C. Lewis, T. Ross, and C. Mendoza, Particle tracks for 'Extreme heterogeneity in the microrheology of lamellar surfactant gels analyzed with neural networks', <https://research.manchester.ac.uk/en/datasets/particle-tracks-for-extreme-heterogeneity-in-the-microrheology-of>.
- [81] <https://github.com/orwm/PTM-with-recurrent-neural-networks>.
- [82] A. Graves and J. Schmidhuber, Framewise phoneme classification with bidirectional LSTM and other neural network architectures, *Neural Networks* **18**, 602 (2005).
- [83] A. C. Tsoi and A. Back, Discrete time recurrent neural network architectures: A unifying review, *Neurocomputing* **15**, 183 (1997).